Available online at www.sciencedirect.com
ScienceDirect
International Journal of Rock Mechanics & Mining Sciences 45 (2008) 1211–1225
International Journal of Rock Mechanics and Mining Sciences
www.elsevier.com/locate/ijrmms

Consolidation settlements above deep tunnels in fractured crystalline rock: Part 2—Numerical analysis of the Gotthard highway tunnel case study

C. Zangerl[a,b,*], E. Eberhardt[a,c], K.F. Evans[a], S. Loew[a]

[a]*Engineering Geology, Swiss Federal Institute of Technology (ETH Zurich), Zurich, Switzerland*
[b]*alpS GmbH, Centre for Natural Hazard Management, Innsbruck, Austria*
[c]*Geological Engineering/Earth and Ocean Sciences, University of British Columbia, Vancouver, Canada*

Received 4 September 2006; received in revised form 21 January 2008; accepted 14 February 2008
Available online 3 April 2008

Abstract

A recent high precision levelling survey several hundred metres above the Gotthard highway tunnel in central Switzerland has revealed up to 12 cm of subsidence. Subsidence of this magnitude in relation to a deep tunnel excavated in fractured crystalline rock is unexpected and appears to be related to large-scale consolidation resulting from groundwater drainage and pore-pressure changes around the tunnel. This is a concern for the 57 km long Gotthard Base Tunnel currently under construction, as its alignment will pass through similar rock mass conditions and under several important concrete dams. Thus, the assessment and prediction of potential surface displacements are of paramount importance. This paper, the second of two parts, presents results from an extensive and thorough numerical modelling study focussing on the hydro-mechanical processes responsible for the measured subsidence above the Gotthard highway tunnel. Results derived from 2-D continuum and discontinuum numerical models (i.e. finite- and distinct-element, respectively) show that discrete fracture deformation and poroelastic consolidation of the intact rock matrix both contribute to the observed subsidence. Moreover, the explicit inclusion of geological structures in the distinct-element models enabled a better fit of the width and shape (asymmetry, small-scale inflections, etc.) of the measured subsidence profile to be achieved. Continuum models, although able to reproduce the maximum settlement when constrained by field observations, could not reproduce the asymmetric shape of the subsidence profile leading to under prediction of vertical displacements away from the centre of the subsidence trough.

Keywords: Rock mass consolidation; Brittle fault zones; Tunnel drainage; Subsidence; Coupled hydro-mechanical behaviour; Gotthard tunnel; Distinct-element method; Poroelasticity

1. Introduction

Recent high precision levelling measurements along the Gotthard Pass road in Central Switzerland have revealed up to 12 cm of subsidence along sections that pass several hundred metres above the Gotthard highway tunnel [1]. Explanations relating to localised surface processes (e.g. a deep, creeping landslide) could be discounted given the absence of local indicators and the 10 km extent over which the settlements were measured. Instead, temporal and spatial relationships between the measured settlements and construction of the Gotthard highway tunnel suggest causality between water drainage into the tunnel and surface deformation (see Figs. 2 and 4 presented in the companion to this paper, hereafter referred to as Part 1).

Surface subsidence relating to fluid extraction or tunnel drainage is commonly experienced in loosely consolidated sediments or high porosity rocks. However, the case involving the Gotthard highway tunnel involves low-porosity ($\leqslant 1\%$ intact matrix porosity), fractured, crystalline rock. Indeed, the measured peak in subsidence coincides with a stiff granitic gneiss unit (the Gamsboden

---

DOI of original article: 10.1016/j.ijrmms.2008.02.002

[*]Corresponding author at: alpS GmbH, Centre for Natural Hazard Management, Grabenweg 3, A-6020 Innsbruck, Austria.
Tel.: +43 512 392929 14; fax: +43 512 392929 39.
E-mail address: zangerl@alps-gmbh.com (C. Zangerl).

1365-1609/$ - see front matter © 2008 Elsevier Ltd. All rights reserved.
doi:10.1016/j.ijrmms.2008.02.005

granite). Subsidence related to deep tunnelling in crystalline rock is generally not recognised as being of significant magnitude to pose a hazard, even though large reductions in pore pressure often occur when driving a deep tunnel. Given the unexpected nature of these settlements and the potential threat such subsidence might pose to the integrity of surface dams lying near the planned alignment of the Gotthard Base Tunnel, currently under construction, an extensive field, laboratory and numerical modelling investigation was performed to explore and explain the mechanisms underpinning the measured subsidence above the Gotthard highway tunnel [1].

This paper presents the results from the detailed numerical modelling study, and focuses on the combined role that brittle fault zones, meso-scale fractures and the intact rock play in promoting consolidation of crystalline rock masses in response to reduced pore pressures through deep tunnel drainage. The paper utilises 2-D numerical models, which are based upon the results of the field investigations and theoretical considerations presented in Part 1. The objective of the modelling is to help identify and rank the importance of the candidate processes and mechanisms responsible for the subsidence. In order to study the individual roles that the discontinuity network and the intact rock matrix may have played in determining the magnitude and shape of the measured subsidence trough, we apply both continuum (finite-element) and discontinuum (distinct-element) numerical techniques.

2. Discontinuum modelling of consolidation subsidence—Gotthard case study

2.1. Model geometry and boundary conditions

The distinct-element code UDEC [2] was used to model the hydro-mechanical coupled processes acting along the mapped discontinuity network (i.e. normal and shear displacement of meso-scale fractures and brittle fault zones), as well as other alternative consolidation mechanisms (e.g. ‘‘Poisson’s ratio’’ effect [3]). The geometry of the ‘‘base model’’ corresponds to a N–S smoothed topographic profile along the Gotthard Pass road (Fig. 1(a)). The profile is approximately centred on the steeply inclined fault zone that yielded the greatest inflow rate during tunnel excavation (~300 l/s). This zone also coincides with the location of the peak in the subsidence trough, suggesting it had a greater influence than the other inflow zones with respect to acting as a major drainage conduit (see Figs. 4 and 5 of Part 1). The inferred transmissivity of this zone and the quantity of water it produced suggest that pore-pressure drawdown penetrated significant distances into the fault zone.

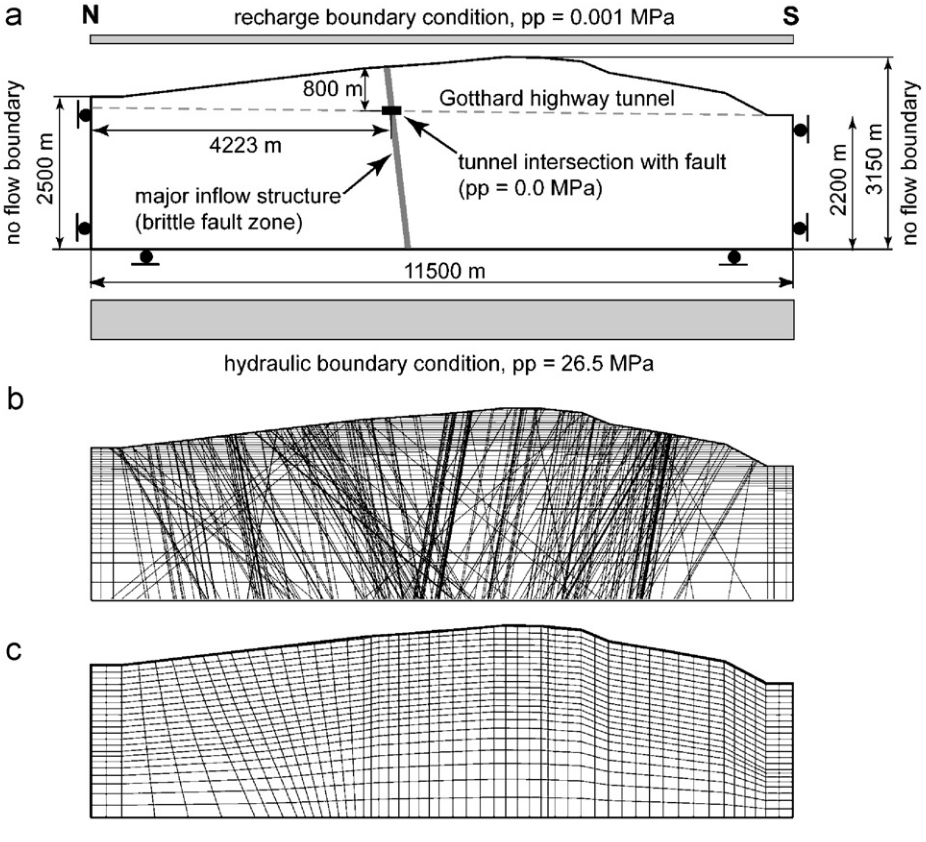

Fig. 1. Modelling of consolidation subsidence for the Gotthard highway tunnel case study, showing: (a) outline of model geometry and ‘‘base model’’ boundary conditions, (b) discontinuum distinct-element model (UDEC) with fracture geometry based on geological structures mapped within the Gotthard highway safety tunnel and on surface, and (c) continuum finite-element mesh (VISAGE).

The boundary conditions applied to the model are also shown in Fig. 1(a). Zero velocity constraints were applied normal to the two sides and base of the model. No-flow hydraulic boundaries were applied along both sides of the model and the base was fixed with a constant pore pressure of 26.5 MPa, corresponding to 500 m of head above the tunnel elevation. This assumption is based on field observations made regarding the regional groundwater conditions, as discussed in Part 1. However, given the inexact nature of certain data (the subsidence was unexpected and therefore detailed before and after measurements were not made), the maximum and minimum values were also modelled. Respectively, these include a constant lower boundary pore pressure set to 30.9 MPa to reflect fully saturated ground conditions (i.e. pore pressures reflecting the maximum model overburden), and a no flow boundary condition (see [1]). Findings from a parametric study [1] suggested that these conditions were amongst the most significant of those assumed that are poorly constrained. To account for surface recharge due to precipitation, constant pore pressures of 0.001 and 0.01 MPa were applied to the upper boundary corresponding to low and high recharge rates, respectively (UDEC does not include provision for a constant flow boundary).

The discrete fractures added to the model were based on direct representations of those mapped underground and on surface as presented in the companion paper (Part 1). The pattern involves a fan-like structure of steeply dipping NE–SW striking brittle fault zones and meso-scale fractures (see Figs. 5–7 of Part 1), for which the plane of symmetry is located close to the maximum measured subsidence value [4].

Practical limitations of computation time and UDEC's representation of discontinuities forced some simplifications to be made in devising a model representation of this network. The brittle fault zones strike roughly perpendicular to the 2-D model profile. Thus, all those mapped in the Gotthard highway safety tunnel could be rendered with the correct location and spacing (Fig. 1(b)). In order to avoid numerical problems relating to extremely low-angle intersections of brittle faults, a regrouping of measured dip angles into three classes of 80°, 60° and 40° was necessary. Faults were assumed to be planar, continuous and sufficiently persistent to extend through the model from the surface to the lower model boundary. Comparison of the orientation distributions of faults mapped in the tunnel and on the surface suggests that they do not steepen or flatten with depth. Of the meso-scale fractures, only a horizontal fracture set, representing the mapped medium- to flat-dipping fractures, were included in the model to avoid unmanageable complexity. The fractures were specified as fully persistent, extending from one model boundary to the other. Whilst this assumption is unrealistic, it nevertheless served to incorporate the key impacts these fractures had on the simulations: i.e. that of providing horizontal connectivity for fluid flow and limiting *in situ* block size. Examination of the simulation results showed there was no tendency for through-going shear to develop on these fractures. Their normal set spacing was set to decrease with depth, in accord with field observations. However, to avoid intolerably long computation runtimes, it was essential to rescale the spacing by reducing the fracture frequency with depth and to compensate by reducing their normal stiffness. This is discussed in the next section.

2.2. Model input parameters

2.2.1. Properties of intact blocks

Model properties for the intact rock blocks were largely based on average values derived from laboratory tests on cores drilled from within the Gotthard highway safety tunnel [1]. The density of the granitic rock was set to 2700 kg/m^3, the bulk modulus to 20 GPa and the shear modulus to 20 GPa (Table 1). These reflect a Young's modulus of 45.5 GPa and a Poisson's ratio of 0.12, as measured in the laboratory.

2.2.2. Normal stiffness of meso-scale fractures and brittle faults

Sensitivity analyses by Zangerl [1] and Zangerl et al. [3] showed that the magnitude of subsidence predicted by the UDEC models is strongly dependent upon the normal stiffness characteristics assigned to the brittle fault zones and sub-horizontal meso-scale fractures. As a result, a detailed literature study of fracture/joint normal deformation behaviour in granitic rocks was undertaken to constrain the range of values modelled. This extensive compilation of normal closure experiments on single unfilled fractures, and the estimation of brittle fault zone normal stiffnesses are presented in a Technical Note [5] and in Appendix A of Part 1. The normal closure characteristics of unfilled fractures are found to be relatively well

Table 1
Intact rock and discontinuity properties for discontinuum distinct-element analysis

Model parameter	Value	
Rock properties		
Density	2700 kg/m^3	
Young's modulus	45.5 GPa	
Poisson's ratio	0.12	
Bulk modulus[a]	20 GPa	
Shear modulus[a]	20 GPa	
Discontinuity properties	*Meso-scale fractures*	*Brittle fault zones*
Normal stiffness	(Stress-dependent)[b]	(Stress-dependent)[c]
Shear stiffness	1 MPa/mm	0.1 MPa/mm
Cohesion	0 MPa	0 MPa
Friction angle	40°	30°
Dilation angle	0°	0°

[a] Calculated from Young's modulus and Poisson's ratio.
[b] See Fig. 2a.
[c] See Fig. 2b.

described by a semi-logarithmic closure law proposed by Bandis et al. [6] and Evans et al. [7]. For this law, the curve of normal stiffness versus effective normal stress is linear and passes through the origin (i.e. zero stiffness at zero normal stress), whereby the normal stiffness can be obtained by

$$k_n = \left(\frac{\mathrm{d}k_n}{\mathrm{d}\sigma'_n}\right)\sigma'_n. \tag{1}$$

The constant, $\mathrm{d}k_n/\mathrm{d}\sigma'_n$, thus completely describes the normal stiffness behaviour of the fracture and is referred to as the "stiffness characteristic" [7]. It follows that the normal stiffness of the fracture, k_n, at any effective normal stress level, σ'_n, can be obtained by multiplying the value of the "stiffness characteristic" by the effective normal stress.

Based on the values obtained from the detailed compilation of published joint normal closure test data [5], a "stiffness characteristics" of $23\,\mathrm{mm}^{-1}$ was used for the horizontal fractures, with a lower bound value of $3\,\mathrm{mm}^{-1}$ taken from the measurement of Jung [8]. Since UDEC implements stress-dependent normal stiffness using a "look-up table" approach, the characteristic curves defined by the "stiffness characteristic" values were discretised into segments of constant normal stiffness, k_n, as shown on the curve for $\mathrm{d}k_n/\mathrm{d}\sigma'_n = 23\,\mathrm{mm}^{-1}$ in Fig. 2(a). As noted earlier, the normal set spacing of the horizontal fractures had to be reduced (i.e. scaled) to maintain numerical efficiency [3]. To compensate for this and preserve net closure, the normal stiffness of the horizontal fractures was similarly reduced. Table 2 lists the measured and rescaled normal set spacings implemented in the UDEC models and the corresponding normal stiffness values for the four depth ranges in which spacing was incremented. The normal stiffness values refer to a fracture with a $\mathrm{d}k_n/\mathrm{d}\sigma'_n$ value of $23\,\mathrm{mm}^{-1}$ supporting a pre-drainage effective vertical stress appropriate for the mid-depth of the range.

Normal stiffness values for the brittle fault zones were generally assumed to be 1 MPa/mm for an effective stress range between 0 and 30 MPa (Fig. 2(b)). At higher effective normal stresses, i.e. between 30–80 and 80–180 MPa, the normal stiffness values were increased to 5 and 10 MPa/mm, respectively. For the lower bound UDEC simulations, normal stiffness values of 0.5, 2.5 and 5 MPa/mm were adopted for stress intervals of 0–30, 30–80 and 80–180 MPa, respectively.

2.2.3. Shear stiffness and strength of meso-scale fractures and brittle faults

The shear stiffness of discontinuities is strongly dependent on the effective normal stress acting across the discontinuity, the size of the fracture sheared, the fracture surface roughness and the nature of the infilling. Large, weak fault zones tend to have low shear stiffness values, perhaps as low as 0.01 MPa/mm, while small fractures are much stiffer, taking values as high as 100 MPa/mm [6].

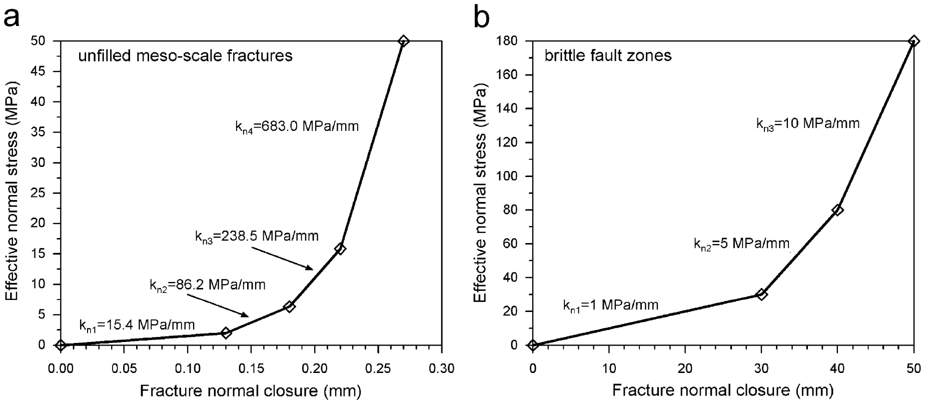

Fig. 2. Normal stiffness curves implemented within the distinct-element models, for: (a) unfilled meso-scale fractures and (b) brittle faults zones.

Table 2
Normal stiffness and spacing of horizontal meso-scale fractures measured *in situ* and the corresponding scaled values implemented in the distinct-element models

Depth range (m)	Effective normal stress range (MPa)	Laboratory and *in situ* measurements		Implemented in UDEC (scaled)	
		In situ spacing (m)	Normal stiffness of single fracture (MPa/mm)	Normal spacing (m)	Equivalent scaled normal stiffness (MPa/mm)
0–600	0–2	1	$k_{n1} = 15.4$	40	$k_{n1} = 0.4$
600–1600	2–6.3	2	$k_{n2} = 86.2$	80	$k_{n2} = 2.2$
1600–2600	6.3–15.9	4	$k_{n3} = 238.5$	160	$k_{n3} = 6.0$
2600–3150	15.9–50	8	$k_{n4} = 683.0$	320	$k_{n4} = 17.1$

Yoshinaka et al. [9] examined scale effects on shear stiffness and found that values increased with decreasing scale from 0.01 MPa/mm *in situ* to 40 MPa/mm in laboratory tests. Guided by these results, the horizontal joints in the UDEC models were assigned a shear stiffness of 1 MPa/mm, and the brittle fault zones were given a value of 0.1 MPa/mm.

The shear strength parameters of the meso-scale fractures were chosen in accord with the results of Barton [10] and Byerlee [11], who report joint cohesions close to zero and joint friction angles between 31° and 42°. For the horizontal fractures, a joint friction angle of 40° was assumed, with a value of 30° assumed for the brittle fault zones. In both cases, the joint cohesion was set to zero. The lower friction angle for the brittle fault zones was suggested by tests conducted on samples from a fault zone several 100 m's thick located in the Tavetsch Massif in Central Switzerland which yielded friction angles of between 24° and 34° [12].

2.2.4. *Transmissivity of meso-scale fractures and brittle faults*

The field evidence and measurements relating to the transmissivity of the meso-scale fractures and brittle fault zones is discussed in Part 1. The field data consist largely of measurements of water inflow into the Gotthard safety tunnel [13]. Six zones of approximately constant hydraulic conductivity were chosen. These are shown in Fig. 3, and the net transmissivity and equivalent porous medium (EPM) hydraulic conductivities of the zones are listed in Table 3. Within the framework of UDEC, flow occurs only in discontinuities whose hydraulic properties are described by hydraulic aperture (the blocks are assumed to be impermeable). Thus, the hydraulic apertures of fractures in each zone were computed from the EPM hydraulic conductivity values and fracture frequency. If a rock mass is cut by parallel fractures with a mean spacing, d_f, each having a hydraulic aperture, a_h, then the EPM hydraulic conductivity, κ, of the rock mass in the plane of the fractures is given by

$$\kappa = \frac{\rho g a_h^3}{12 \mu d_f}, \tag{2}$$

where ρ is the water density, g is the acceleration of gravity and μ is the dynamic viscosity of the water. All fractures/faults within a zone were assumed to have the same hydraulic aperture. Values for the brittle fault zones and meso-scale fractures are listed in Tables 3 and 4, respectively.

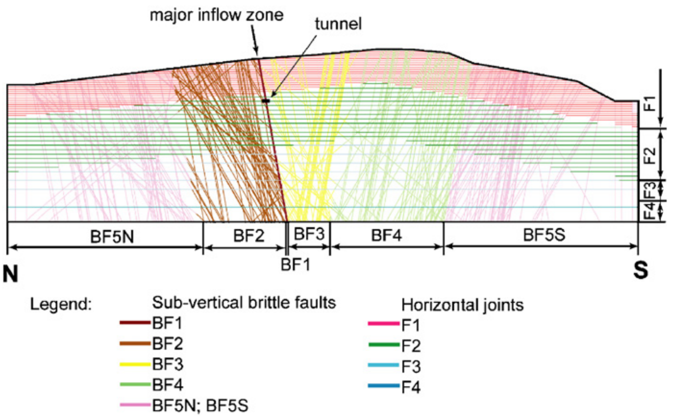

Fig. 3. Discontinuity pattern and applied hydraulic transmissivities used in the discontinuum analysis (i.e. distinct-element) of the Gotthard highway tunnel case study. Transmissivities are based on mapping and inflow observations made from within the tunnel. Horizontal joint (F#) and brittle fault zone (BF#) designations correspond to those given in Tables 3 and 4.

Table 3
Net transmissivity and EPM hydraulic conductivity of the rock mass section intersected along the Gotthard safety tunnel corresponding to the regions shown in Fig. 3

Region[a]	Net transmissivity along tunnel intersection (m^2/s)	EPM vertical hydraulic conductivity (m/s)	Initial hydraulic aperture of each fault (mm)
1 (BF5N)	3.0e−6	1.2e−9	0.037
2 (BF2)	1.8e−5	1.1e−8	0.074
3 (BF1)	2.4e−4	9.1e−6	0.459
4 (BF3)	9.6e−6	6.3e−9	0.070
5 (BF4)	5.0e−6	2.4e−9	0.046
6 (BF5S)	3.0e−6	1.2e−9	0.037

The hydraulic aperture gives the value that must be ascribed to all faults that intersect the tunnel over the region to produce the given transmissivity.

[a] see Fig. 3.

Table 4
Hydraulic properties of horizontal meso-scale fractures

Depth range[a] (m)	Fracture vertical spacing (m)	EPM horizontal hydraulic conductivity (m/s)	Fracture hydraulic aperture (mm)
F1: 0–600	40	1e−7	0.170
F2: 600–1600	80	1e−8	0.099
F3: 1600–2600	160	5e−9	0.099
F4: 2600–3150	320	3e−12	0.011

[a] See Fig. 3.

2.2.5. *Initial stress conditions*

The state of stress in the Gotthard region is poorly constrained. Regional stress determinations derived from inversions of earthquake focal mechanisms in neighbouring regions (the Gotthard region is largely aseismic) by Kastrup et al. [14] suggest that the minimum horizontal principal stress across much of northern and eastern Switzerland is less than the vertical stress and oriented approximately NE. However, it is the magnitude of the orthogonal horizontal principal stress in the NW direction, σ_{NW}, that primarily determines the stress ratio required for the 2-D plane of reference modelled. We shall refer to this stress ratio as $R_{NW} = \sigma_{NW}/\sigma_V$. Unfortunately, the inversions performed in [14] suggest that R_{NW} varies strongly from region to region, being greater than 1.0 to the north and west of the study area and less than 1.0 to the south. Thus, the horizontal to vertical stress ratio for the modelling was nominally taken to be 1.0, but variations between 0.5 and 2.0 were also considered to assess its impact on the model results (as described in the next section).

2.3. Sensitivity analysis of poorly-constrained parameters

Most of the required UDEC model input parameters could be reasonably constrained by data collected during the field investigation. However, several parameters were judged to be poorly constrained either due to excessively large ranges in values obtained from laboratory testing, scale dependency problems, or because representative values taken from the literature were used. For these parameters, sensitivity analyses were performed to determine the impact of their uncertainty on the modelling results and to aid in preparing the main model runs reported in the next section. The sensitivity analyses were performed on simple model geometries each designed to highlight the specific effect attributable to the parameter in question. The model geometries, boundary conditions, material properties and the results of this comprehensive parametric study are presented in detail in [1].

The parametric study showed that the model results are only partly sensitive to changes in the value of the intact rock bulk modulus, with a difference of 1 cm (from 36%) in predicted subsidence between the lower and upper bound values of 20 and 60 GPa (or Poisson's ratio of 0.13 and 0.35). This change can be ascribed to the "Poisson's ratio" effect described in [3], which involves vertical block contraction/shortening due to horizontal block expansion upon vertical fracture closure.

A similar degree of sensitivity was seen in the results of varying the horizontal-to-vertical stress ratio (R_{NW}) between 0.5 and 2.0. For models characterised by inclined fractures, a decrease of 35% in peak subsidence was modelled when R_{NW} was increased from 0.5 to 2.0 due to the greater shear displacements driven by the higher resolved shear stresses and lower effective normal stresses acting on the inclined faults in the model. Little effect on subsidence was observed for model geometries based on horizontal joints and vertical faults (in the case of the latter, this is due to the assumed stress-independence of the normal stiffness of the fault zones).

Increased shear displacements on the inclined faults were also observed when their shear stiffness value was decreased, enabling increased elastic shear displacements. Decreasing the shear stiffness of the inclined faults by two orders of magnitude (from 1 to 0.01 MPa/mm) resulted in an increase of 3.5 cm in the modelled peak subsidence, whereas the same change for the vertical faults only produced an increase of 0.4 cm.

A more significant increase of 2 cm was seen when the normal stiffness of the vertical faults was decreased (from 10 to 0.1 MPa/mm). In general, subsidence is less sensitive to the normal stiffness of vertical discontinuities, because their closure only generates vertical subsidence through the above noted "Poisson's ratio" effect. The closure of horizontal joints through drainage, however, directly contributes to vertical displacements and so in this case, the normal stiffness can be a highly sensitive parameter. Results show that varying the normal stiffness of the horizontal fractures by two orders of magnitude can produce differences in the modelled surface subsidence equal to the magnitudes measured.

The final input parameter tested with respect to model sensitivity, in order to prepare the main model runs, was the effect of permeability anisotropy within the discontinuity network. This was examined by systematically varying the hydraulic apertures so as to affect a change in the horizontal-to-vertical EPM hydraulic conductivity ratio (i.e. κ_h/κ_v) of the simulated rock mass. Varying the κ_h/κ_v ratio from 0.001 to 1.0 led to distinctive differences in the pore-pressure distribution after tunnel drainage, which in turn influenced the shape of the subsidence profile and magnitude of surface subsidence (increasing by 2 cm).

2.4. Discontinuum (UDEC) modelling results

Based on the findings of the parametric sensitivity analysis, a "base-model" simulation was defined whose geometry is shown in Figs. 1(b) and 3 and whose parameters are listed in Tables 1–4. The model was time-stepped to initialise the mechanical equilibrium and steady-state flow conditions that prevailed prior to tunnel excavation. The pore-pressure distribution for the initial conditions (i.e. 0.001 and 26.5 MPa constant pore-pressure boundaries along the surface and base of the model, respectively) is shown in Fig. 4(a). Since this corresponds to a head of 500 m above the tunnel level, a hydraulic potential is defined across the model that drives downward steady-state flow. This tends to be locally drawn towards the major inflow zone, BF1, because of its higher transmissivity (Fig. 3), generating a local depression of the pore-pressure contours around the fault near the bottom of the model (Fig. 4a).

Next, a hydraulic sink is introduced by setting the pore pressure to zero at the point marking the intersection of the tunnel with the major inflow zone (as indicated in Figs. 1 and 3). The resulting steady-state pore-pressure distribution after solving for the tunnel drainage condition is shown in Fig. 4(b). This shows that after tunnel drainage is permitted, the pore-pressure contours become markedly drawn down within and about the BF1 fault zone structure, and the pressure gradient driving downward flow within the fault zone above the tunnel drops to very low levels, reflecting the high transmissivity of the feature. Below the tunnel level, the pore-pressure disturbance about the fault progressively diminishes to pre-drainage levels. Fig. 4(c) shows the pore-pressure drawdown contours in

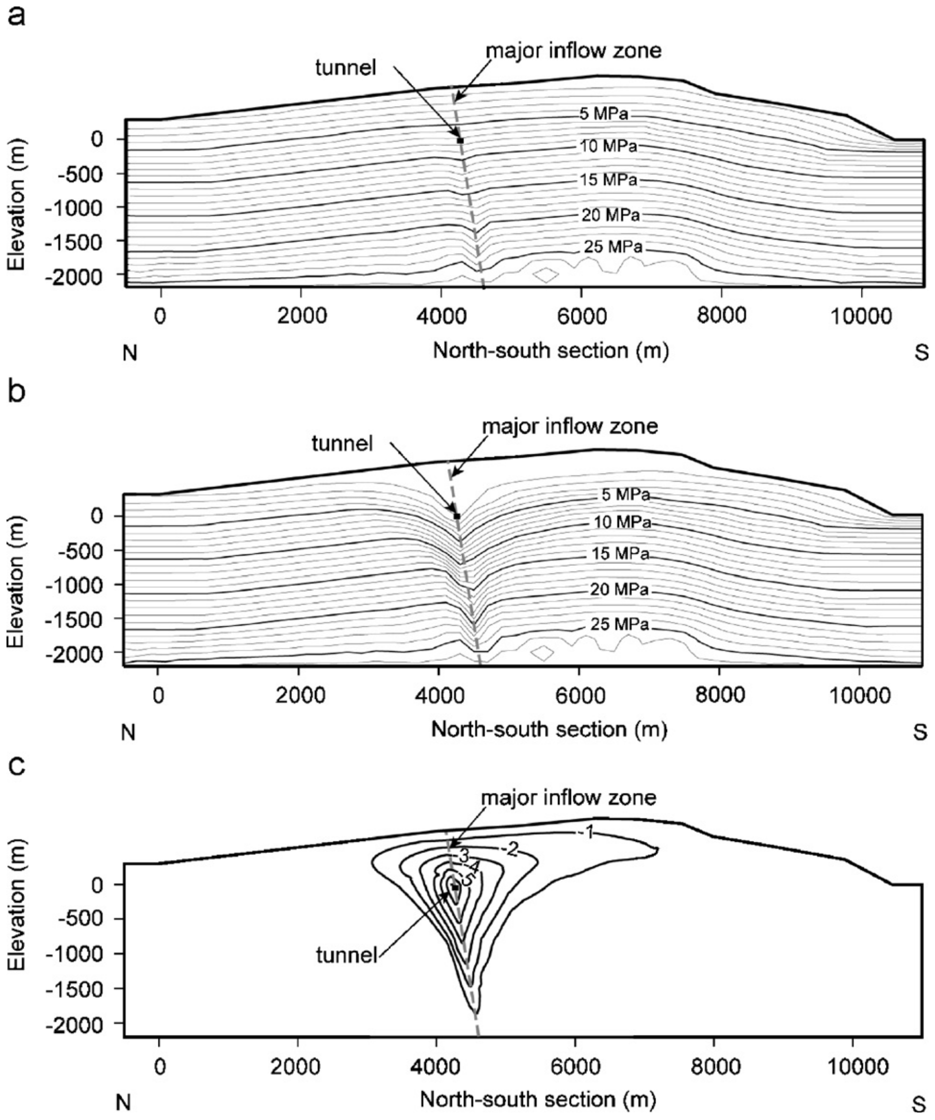

Fig. 4. Pore-pressure distributions: (a) before and (b) after tunnel drainage, derived for the discontinuum distinct-element analysis. (c) Pore-pressure drawdown contours (in MPa) within the rock mass calculated from the initial and drained situation. Note that the axis of the tunnel at the drainage zone was set to 0 m (and represents 1169 m above sea level).

MPa resulting from the pore-pressure difference between the initial and the tunnel-drained rock mass conditions.

Contours of vertical displacement generated by the effective stress changes that accompany drainage into the tunnel for the base model are shown in Fig. 5(a), and the corresponding profile of surface subsidence in Fig. 5(b). Vertical strains arise from closure of the horizontal joints together with the closure of faults which, because they are mostly steeply inclined, allow the intact blocks to expand laterally. This generates vertical contraction strain through the Poisson's ratio effect [3] noted previously. The maximum predicted subsidence of 0.042 m occurs several hundred metres to the south of the major inflow zone due to complex topographic, structural and hydraulic conductivity effects (Fig. 5). The subsidence trough has a predicted width of about 8500 m, with subsidence values greater than 0.01 m occurring over an area that is more than 4500 m wide. The slight vertical uplift evident some 2000 m north of the major fault zone may be related to the shear slip on the faults that dip to the north. Shear deformations on faults and fractures, predominately of elastic type, are also indicated in Fig. 5(a). Minor shear displacements along the right and left model boundaries are related to boundary effects. Within the central subsidence trough, shear displacements of up to 4 mm occur on specific faults. Contours indicating the closure of the brittle fault zones are shown in Fig. 6 and reach magnitudes of 5 mm near the tunnel.

Fig. 7(a) shows the predicted subsidence profiles obtained by varying several select parameters (based on the findings of the sensitivity analysis). These can be compared with the width, asymmetry and small-scale inflections of the measured subsidence profile along the Gotthard Pass road shown in Fig. 7(b). The maximum

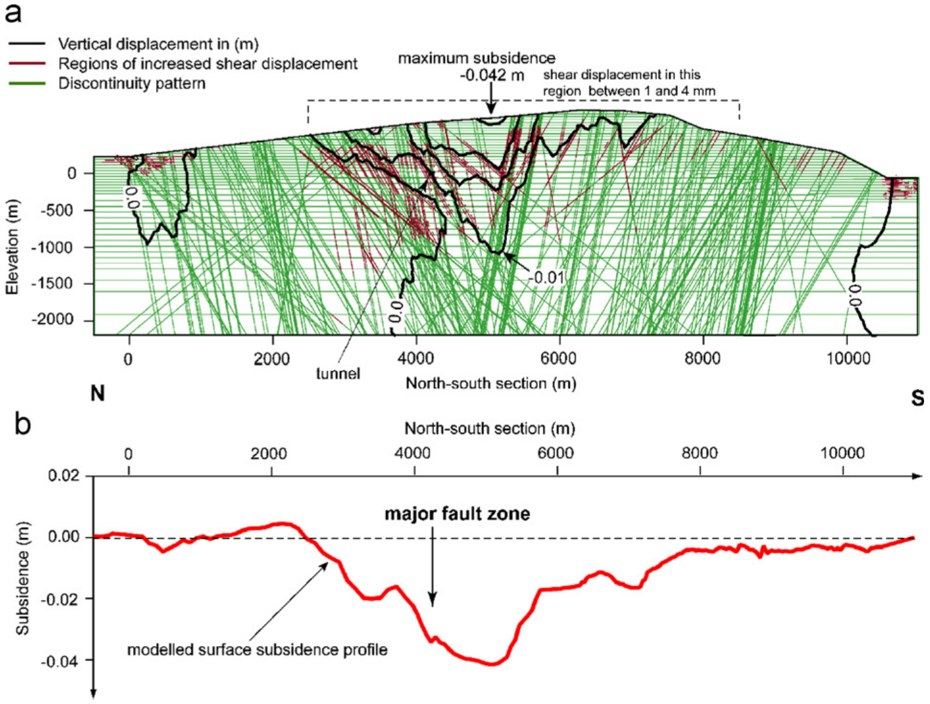

Fig. 5. Discontinuum distinct-element model results showing: (a) contours of vertical displacements and shear displacements along steeply inclined fault zones and (b) resulting modelled surface subsidence profile.

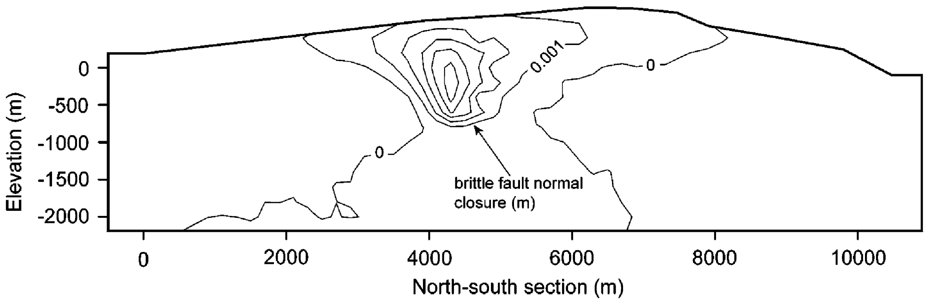

Fig. 6. Discontinuum distinct-element model results showing normal closure along sub-vertical fault zones.

subsidence of 8.0 cm was obtained from a model in which the normal stiffnesses of both the fault zones and the horizontal fractures involved lower bound values. Specifically, the normal stiffness of the fault zones was reduced from 1, 5 and 10 MPa/mm segments (according to the effective stress intervals shown in Fig. 2(b)) to 0.5, 2.5 and 5 MPa/mm, and the "stiffness characteristics" of the horizontal fractures was set to $3\,\mathrm{mm}^{-1}$ (denoted as the "low normal stiffness model"). A higher surface recharge, simulated by increasing surface pore pressure from 0.001 to 0.01 MPa, reduced the maximum subsidence by 1 cm (denoted as the "high surface recharge model", Fig. 7(a)).

As demonstrated in Fig. 7, the discontinuum-based distinct-element models were able to reproduce most of the asymmetry and small-scale inflections with respect to the shape of the subsidence profile. However, they were unable to explain the total surface settlement magnitudes measured above the Gotthard highway tunnel. These aspects of the discontinuum results and their significance are explored later in the discussion.

3. Continuum modelling of consolidation subsidence—Gotthard case study

One of the major limitations of UDEC's distinct-element formulation is that the intact blocks are assumed to be impermeable, devoid of connected porosity. In practice, they have connected porosities in excess of the 1% measured on core samples, and are permeable on sufficiently long timescales. Hence, given time, they will undergo the same pore-pressure drawdown as the bounding fractures. Such drawdown will lead to compaction of the blocks that will add to the surface subsidence. To assess the magnitude of this component of subsidence, the finite-element continuum code VISAGE [15] was used to analyse the poroelastic consolidation obtained from the intact rock

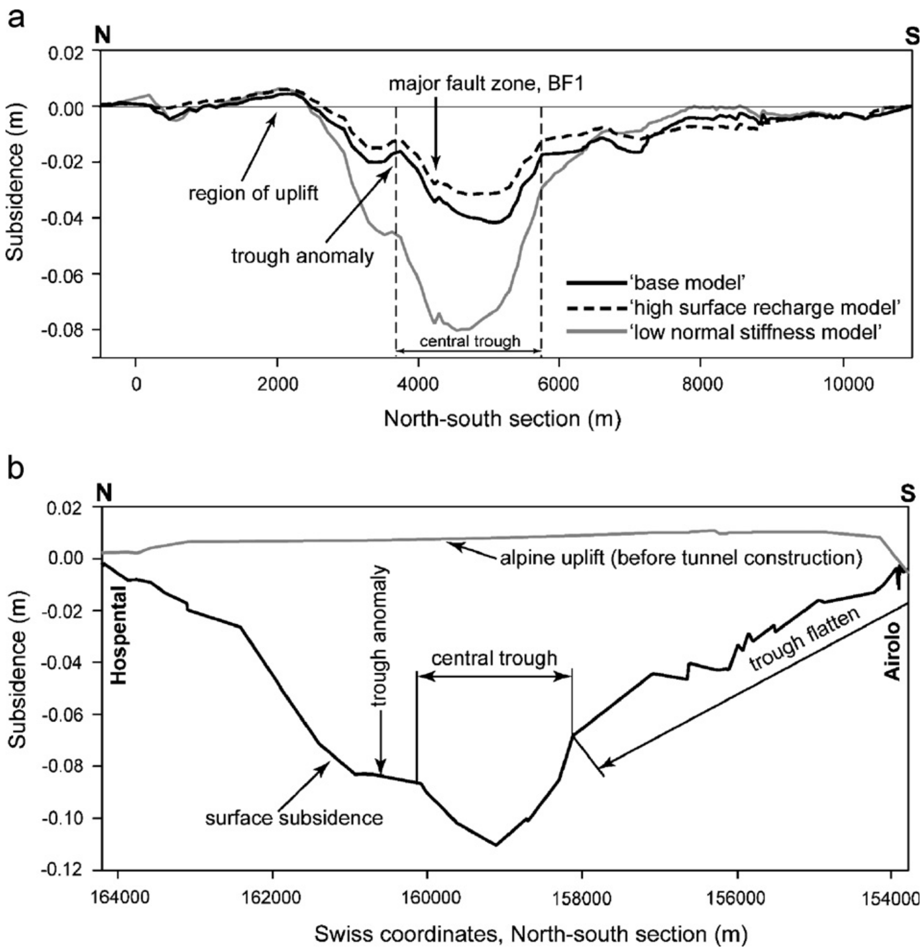

Fig. 7. (a) Modelled surface subsidence profile focussing on fracture consolidation adopting a discontinuum approach (i.e. distinct-element method). (b) Levelling profile along the Gotthard Pass road showing surface subsidence.

block matrix. The theoretical background for this process is given in Part 1.

3.1. Model geometry and boundary conditions

The same model geometry and boundary conditions were used for the VISAGE continuum analysis as for the UDEC discontinuum analysis to permit direct comparison of the results (Fig. 1(a)). The finite-element mesh is shown in Fig. 1(c) and consists of 4810 nine-noded higher-order quadrilateral elements. Initial pore pressure and *in situ* stress conditions were the same as those used for the UDEC base model. After initial model consolidation, pore-pressure drawdown due to tunnel drainage was initiated by setting the pore pressure to zero at nodes where the tunnel intersects the major inflow fault.

3.2. Model input parameters

The finite-element solution of Biot's consolidation theory (see Part 1) used in VISAGE requires as input seven independent parameters: water density, rock density, drained Young's modulus, drained Poisson's ratio, Biot's constant, Skempton's constant and the hydraulic conductivity. Wherever possible, material properties were assigned values identical to those used for the intact rock blocks in the UDEC discontinuum analysis. These properties are summarised in Table 5. Thus, the medium is considered to be composed of intact granite, in contrast to the medium used for the analytic poroelastic calculations in Part 1 where the properties were assigned to reflect bulk properties (i.e. including the effects of both fractures and intact rock). Material properties were assumed to be isotropic

Table 5
Rock mass properties for continuum finite-element analysis where the rock mass is represented as a homogeneous, isotropic medium

Parameters	Value
Rock density (kg/m^3)	2700
Fluid density (GPa)	1000
Young's modulus (GPa)	45.5
Poisson's ratio	0.12
Hydraulic conductivity (m/s)	1e−8
Biot's coefficient	0.70
Skempton's coefficient	0.92

and homogeneous throughout the modelled continuum in the VISAGE base model. However, several models were run that used depth-dependent elastic moduli and poroelastic coefficients (Table 6). Hydraulic conductivity was assumed isotropic and for the most part set to 1×10^{-8} m/s (Tables 5 and 6). These conductivity values are appropriate for the bulk fractured rock mass, and serve the purpose of generating drawdown distributions similar to those in the UDEC modelling.

3.3. *Continuum (VISAGE) modelling results*

Pore-pressure distributions at steady state for the continuum base model with isotropic hydraulic conductivity before and after tunnel drainage are shown in Figs. 8(a) and (b), respectively. The corresponding subsidence profile is shown in Fig. 9 and is symmetric about the point of tunnel drainage with a maximum value of 6.0 cm. The distribution of pore-pressure drawdown due to tunnel

Table 6
Rock mass properties for continuum finite-element analysis using depth-dependent (i.e. stress-dependent) elastic properties

Parameters	0–200 m	200–400 m	400–800 m	800–1400 m	>1400 m
Density (kg/m^3)	2700	2700	2700	2700	2700
Young's modulus[a] (GPa)	45.5	45.5	45.5	45.5	45.5
Young's modulus[b] (GPa)	20	23.5	27.0	32.9	45.5
Poisson's ratio	0.12	0.12	0.12	0.12	0.12
Hydraulic conductivity (m/s)	1e−8	1e−8	1e−8	1e−8	1e−8
Biot's coefficient	0.70	0.65	0.55	0.5	0.25
Skempton's coefficient	0.92	0.90	0.85	0.83	0.62

[a] Constant.
[b] Stress dependent.

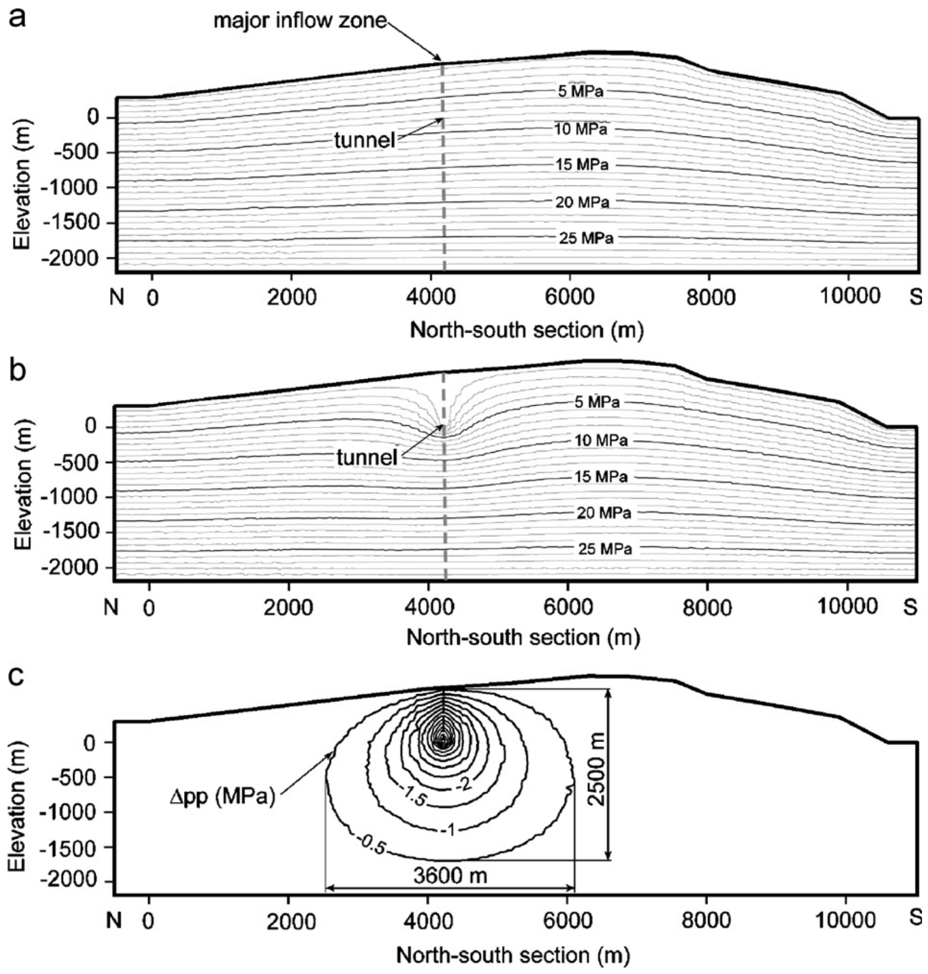

Fig. 8. Pore-pressure distributions derived for the continuum finite-element analysis: (a) before tunnel drainage, (b) after tunnel drainage assuming isotropic hydraulic conductivities and (c) continuum finite-element derived pore-pressure difference between initial and tunnel-drained conditions.

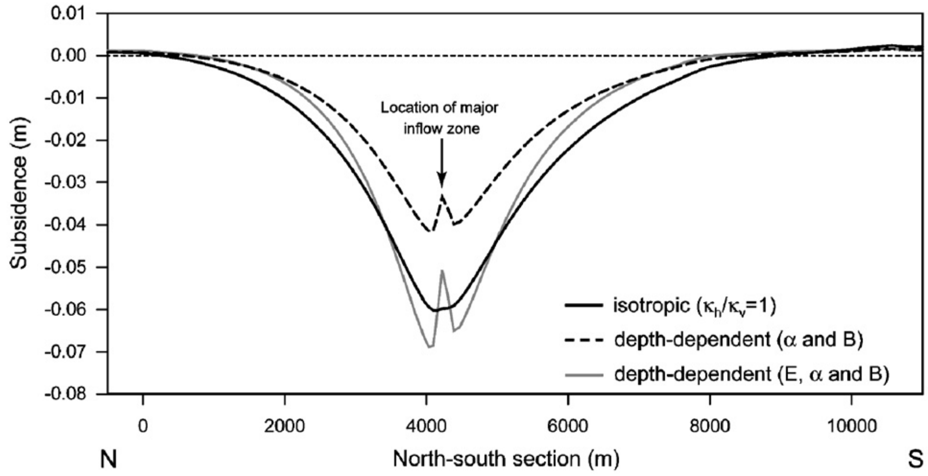

Fig. 9. Modelled subsidence profile focussing on intact rock consolidation adopting a continuum approach (i.e. finite-element method).

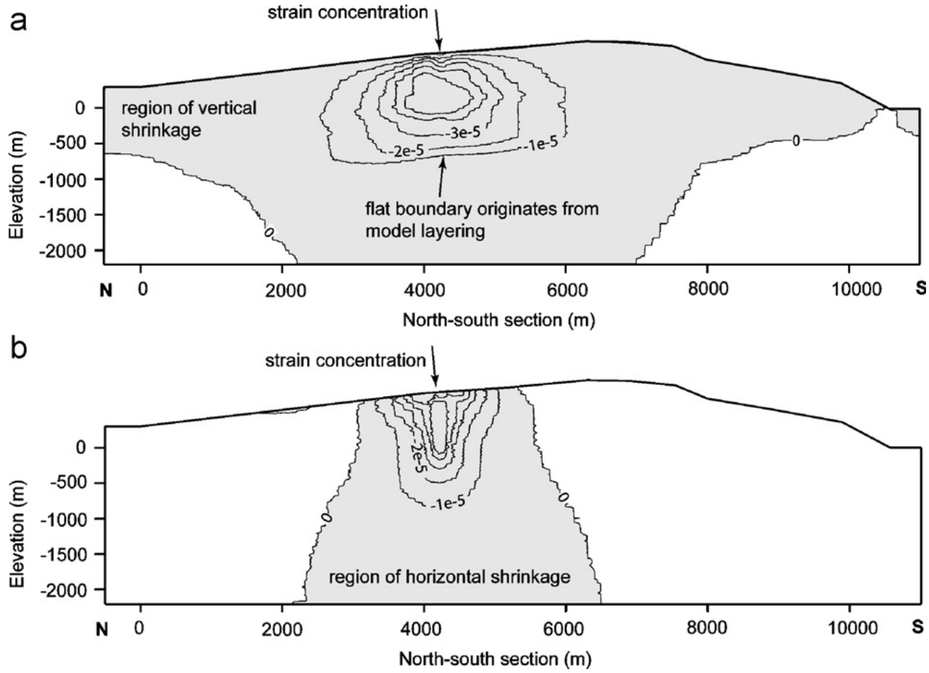

Fig. 10. Continuum finite-element derived distribution of intact rock strains, showing: (a) vertical strains and (b) horizontal strains.

drainage is shown in Fig. 8(c). Drawdowns of up to 0.5 MPa extend laterally 3600 m and vertically 2500 m from the tunnel. The mean drawdown within this region is 1.6 MPa (Fig. 8(c)).

The effect on the predicted subsidence curve from using the depth-dependent Biot and Skempton coefficients (Table 6) is shown as a dashed-line curve in Fig. 9. All other parameters are assumed to be homogeneous and isotropic. The maximum subsidence is reduced to 4.2 cm although the form of the curve is unchanged, because the pore-pressure distribution (not shown) is similar in symmetry, shape and extent to that for the isotropic continuum base model. If the Young's modulus is also assigned depth-dependent values (as given in Table 6) then the peak subsidence increases to 6.8 cm (Fig. 9). The effect of the more compliant surface layers is to focus the deformation resulting in a narrower central trough. Vertical and horizontal strain contours, depicted in Fig. 10, show that both horizontal and vertical contraction occurs in the vicinity of the conductive/draining vertical fault zone.

4. Discussion

4.1. Structural controls in determining the shape of the subsidence trough

One of the key differences between the results of the discontinuum and continuum model simulations was the predicted shape of the subsidence trough. It should be recalled that the objectives behind each modelling approach were complementary but different: the discontinuum analysis was concerned with highlighting the consolidation that arose from dislocation (normal and shear) of the discontinuity network, whereas the continuum analysis focussed on the consolidation of the bulk intact rock blocks (see Fig. 10 in Part 1). Results obtained from the continuum analysis produced a subsidence profile that for the most part was symmetrical about the point of tunnel drainage (Fig. 9). In contrast, the shape of the subsidence trough calculated in the distinct-element simulations reproduced both the general asymmetry and several key inflections seen in the measured subsidence profile (Fig. 7). This agreement was the direct result of the explicit inclusion of the major mapped fault zone structures, both in terms of location and orientation. The key features in the subsidence profile and their origin as suggested by the modelling are as follows (Fig. 7):

(a) The steeply inclined central part of the trough, approximately 2000 m in width (from tunnel chainage 3800–5800 m) may be derived from the regional fan-shaped alignment and structure of the brittle fault zones. The point where the dip reverses direction corresponds exactly with the location of maximum subsidence. The boundaries between the central and outer trough coincide with clusters of brittle faults, which underwent shear displacement in the model (Figs. 5 and 7).

(b) A 600 m wide inflection in the subsidence curve occurs 1000 m north of the peak (tunnel chainage 3200–3800 m). As discussed later, this feature coincides with the location of an isolated cluster of water-bearing faults intersected in the tunnel (Fig. 11), suggesting localised, enhanced drainage of pore pressure may be responsible. However, it is also possible that the inflection is structurally controlled through the orientation and high frequency of the fault zone pattern. The modelling shows that several steep, south-dipping clusters of closely spaced fault zones affect the trough through variations in the elastic shear and normal closure displacement. Three medium to north dipping fault zones are observed that may additionally influence the shape of the trough through north-directed shear displacements. In general, the fault zone frequency is found to be significantly higher than in the central trough and north of this zone.

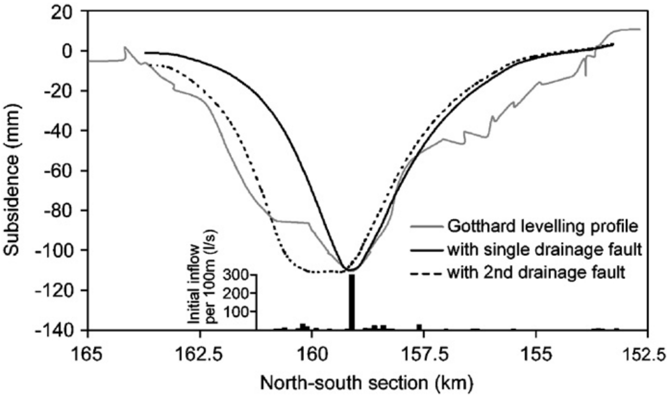

Fig. 11. Gotthard subsidence profile and those modelled assuming additional key drainage fault structures (after [16]). In addition measured initial inflow rates into the Gotthard highway safety tunnel near the peak subsidence were shown (initial inflow rates per 100 m interval).

(c) The shoulder that marks the south boundary of the central trough coincides with increased shearing on north dipping fault zone clusters (tunnel chainage 6000 m). Beyond this shoulder, the slope flattens and the magnitude of subsidence reduces gradually, reflecting diminishing drawdown of pore pressure.

(d) Fluctuations/inflections along the flattened southern limb are caused in the model by non-uniform shear deformation along several south-dipping faults in a fault domain where the dip direction is predominantly to the north.

In summary, the detailed geometry of the subsidence profile indicates the involvement of predominately elastic shear and normal displacements on mapped fault zones in the formation of the subsidence trough. As such, it can be inferred that the geological anisotropy plays a significant role in influencing the shape of the trough. This is likewise true with respect to the influence of additional permeable fault zones intersecting the tunnel. Eberhardt et al. [16] performed further continuum models with a second water-bearing fault zone. The numerical models presented here only incorporated a single drainage structure coincident with the point of maximum inflow (i.e. 300 l/s, Figs. 4b and 7 in Part 1). However, Fig. 4b in Part 1 also shows that an additional grouping of water-bearing fault zones (the largest producing >30 l/s) were intersected approximately 1100 m to the north of the 300 l/s major inflow interval. Fig. 11 shows the continuum model results when these drainage points are also incorporated into the model (in this case modelled as an equivalent rock mass where the properties of the discontinuities are also included). A better fit in terms of the width of the settlement trough is achieved through the inclusion of the second draining fault zone; however, the asymmetry and shape anomalies are still not captured.

4.2. *Consolidation of fractured crystalline rock masses*

The results of the analysis clearly demonstrate that fracture closure alone is not the only subsidence producing mechanism, but that the intact rock matrix can contribute considerably to rock mass deformation through poroelastic strains. The latter process is governed by the gradual decline of pore pressure in the intact blocks to maintain equilibrium with the drawn-down pressure in fractures/faults that bound them. As such, the subsidence process can be sub-divided into two separate, albeit coupled deformation mechanisms. During the initial stage of rock mass drainage, discontinuity deformation is the predominant compaction mechanism and can be characterised by closure and minor shear of horizontal fractures, closure and significant shear along sub-vertical and inclined brittle fault zones, and undrained straining of the intact blocks (largely, horizontal extension and vertical contraction) as a consequence of closure of their bounding discontinuities. Results from the parametric study show that the magnitude of subsidence predicted by the model is most strongly dependent upon the frequency and normal stiffness of sub-horizontal fractures. However, the normal stiffness ascribed to steeply inclined, brittle fault zones also significantly affects the predicted subsidence magnitude and trough shape through a "Poisson's ratio" effect. At later times, drawdown of fluid pressure in the discontinuity network penetrates the intact blocks, generating compactional strains through poroelastic coupling. Parametric analyses of the effect show the predicted magnitude of subsidence is most strongly affected by the elastic material properties (i.e. Young's modulus and Poisson's ratio, or the bulk and shear modulus), and the pore pressure–stress coupling (i.e. Biot's coefficient, α).

In reality, the deformations arising from the discontinuity closure and compaction of intact blocks are coupled. Thus, the subsidence arising from the two processes will not simply be the sum of the curves derived from the two processes acting alone (discontinuum and continuum). For example, including intact block compaction due to internal drawdown in the UDEC discontinuum models, if it were possible, would generate larger reductions in horizontal stress that could drive greater shearing on the faults, as well as directly adding to the vertical consolidation strain.

Overall, the results from the discontinuum and poroelastic-continuum models clearly show that the measured surface subsidence of 12 cm above the Gotthard highway tunnel cannot be explained through discontinuity deformation alone, nor through consolidation of relatively intact rock blocks alone. Instead, subsidence within the fractured granitic rock mass appears to involve significant contributions from both deformation mechanisms, as summarised in Table 7. Some 4–5 cm of subsidence could be explained though fracture driven processes when the most reasonable input parameters were used, whereas compaction of intact blocks could reasonably account for a further 5–6 cm.

4.3. Limitations arising from simplification of the hydraulic properties of structures

Observations made during the driving of the Gotthard safety tunnel suggest that the major inflow zone initially produced ~300 l/s and then declined to a steady-state inflow rate of ~8 l/s. In principle, these observations impose significant constraints on both discontinuum and continuum models alike, particularly with regard to the hydraulic properties of the major inflow fault zone and the surrounding medium. However, applying them to 2-D models is rather complicated, since the length of the faults zone along strike is not specified and the flow into the tunnel involves convergence of the flow field (i.e. radial flow). A further difficulty is given by the need to approximate surface recharge as a constant pressure boundary condition in UDEC, rather than constant flow. Because of these problems, flow rates into the tunnel could not sensibly be used as a quantitative constraint in the modelling. This masked an important deficiency in the representation of the major inflow fault zone. In each of the UDEC and VISAGE models, the draining fault structure was assumed to extend from the surface to the bottom of the model, and to have a uniform transmissivity given by

Table 7
Summary of results showing maximum subsidence generated from the discontinuum distinct-element treatment of the discontinuity network, and the continuum finite-element treatment of the intact rock block matrix

	Underlying deformation mechanisms	Maximum subsidence (m)	Comments
Discontinuum (discontinuity network)	Normal and shear deformation along discontinuities; "Poisson's ratio" effect involving horizontal expansion and vertical contraction of intact rock blocks in response to pore pressure decreases along vertical fractures	0.042	Surface recharge: pp = 0.001 MPa
		0.032	High surface recharge: pp = 0.01 MPa
		0.080	Exceptional low k_n of faults and fractures
	Range	**0.032–0.080**	
Continuum (intact rock block matrix)	Poroelasticity of the intact rock matrix (isotropic permeability)	0.060	E and α, B = constant
	Poroelasticity of the intact rock matrix (depth-dependent parameterisation)	0.042	E = constant; α and B depth-dependent
	Poroelasticity of the intact rock matrix (depth-dependent parameterisation)	0.068	E and α, B depth-dependent
	Range	**0.042–0.068**	

pp, pore pressure; k_n, fracture normal stiffness; E, Young's modulus; α, Biot's coefficient; B, Skempton's coefficient.

the high value of 2.2×10^{-4}–2.6×10^{-4} m^2/s measured at its intersection with the tunnel. However, such a high value would result in a steady-state inflow of fluid much greater than 8 l/s if the groundwater table is maintained at near pre-disturbance levels, as suggested by the presence of springs on the surface. Given that it is probable that the fault zone in question is sufficiently extensive to outcrop at the surface, the observations are best explained by heterogeneity in the transmissivity of the fault zone such that downward flow from the level of the groundwater table at 2300 m a.s.l. (see Part 1) experiences greater impedance than is inherent in the present models. Whilst this would have some impact on the distribution of drawdown within the rock mass, the changes would not be sufficiently pronounced to radically alter the subsidence profile.

4.4. *Recommended monitoring programs*

Given the lack of prior treatment/consideration of consolidation effects in crystalline rock masses in relation to large tunnelling projects, the lessons learned from this study have significant implications for similar future tunnelling projects worldwide. Already, small surface displacements, including vertical settlements as well as horizontal strains, have been recorded close to the Nalps dam in relation to the Swiss AlpTransit Gotthard Base Tunnel excavations near Sedrun [17]. If such displacements develop towards critical values (e.g. a few tens of centimetres change in length along the crest line of an arch dam), then tunnelling operations may be forced to cease causing expensive delays and intervention measures like high pressure grouting.

Findings from this study demonstrate the importance for high precision and continuous spatial and temporal deformation and tunnel inflow measurements over the course of the tunnel excavation. Sensitivity analyses of the rock mass compressibility (storativity), hydraulic conductivity and surface boundary conditions confirm the strong dependency of the resulting modelled subsidence profile, in terms of shape, extent and magnitude, on the final drained pore-pressure response and rock mass structural heterogeneity and compressibility. One of the major limitations to the present case study of the Gotthard highway tunnel was that the pore-pressure drawdown due to tunnel drainage was not well constrained. Prior to construction, the prospect of generating critical surface displacements several hundred metres above the tunnel (in crystalline rock!) was not considered, and therefore data relating to the pore-pressure evolution were not recorded. This is in contrast to cases relating to reservoir compaction and surface subsidence due to oil or water extraction where such effects are expected from the beginning (e.g. [18, 19]).

Ideally, it would have been preferable to have rock mass pore water pressures monitored before, during and after construction of the Gotthard highway tunnel. Installation of a deep pore-pressure monitoring system would provide the best means to address these key shortcomings; however, the technical difficulties and high costs associated with their installation would likely prohibit their use. Direct measurement of rock strain along boreholes would likewise provide much needed insight into the contributions of the different structural elements (i.e. meso-scale fractures, fault zones and intact rock blocks) to the integrated surface deformations and corresponding model constraints.

5. Conclusions

Geomechanical modelling of surface settlements measured above the Gotthard highway tunnel in Switzerland demonstrate that drawdown of pore pressures in deep, crystalline rock masses through tunnelling activity can result in consolidation of the rock mass, generating surface settlements of sufficient magnitude and extent to pose a threat to the integrity of strain-sensitive surface structures (e.g. thin-arch concrete dams).

Results from the numerical analyses presented, using distinct-element discontinuum and finite-element poroelastic continuum models, indicate that the measured surface subsidence of 12 cm above the Gotthard highway tunnel cannot be explained through discontinuity deformation alone, nor through consolidation of relatively intact rock blocks alone. Instead, subsidence within the fractured granitic rock mass appears to involve significant contributions from both deformation mechanisms. Some 4–5 cm of subsidence could be explained through fracture driven processes when the most reasonable input parameters were used, whereas compaction of intact blocks could reasonably account for a further 5–6 cm.

Studies using the discontinuum models, which served to illuminate the role of faults and fractures, showed that the frequency and the normal stiffness of sub-horizontal fractures have the largest impact on the magnitude of vertical settlements induced through tunnel drainage. Closure of high-angle fractures and brittle fault zones, which constitute the vast majority of the major discontinuities in the rock mass, produce subsidence only indirectly through a Poisson's ratio effect. However, shear slip on these structures had a considerable affect on the shape and localised variations in the subsidence profile. In general, the distinct-element models proved to be most effective with respect to reproducing the asymmetry and small-scale inflections in the measured subsidence profile.

Studies using the continuum models, which focussed on establishing the contribution to the subsidence of the intact rock matrix through poroelastic strains, showed that the related steady-state subsidence magnitudes were primarily controlled by the values of the drained bulk modulus and Biot's coefficient of the intact material. At greater depths, where fracture-based deformation diminishes due to increasing normal stiffnesses, the contribution of the intact matrix on the total rock mass deformation becomes more relevant.

Acknowledgements

The authors would like to thank the maintenance team of the Gotthard highway tunnel for their kind support of this work and the AlpTransit Gotthard AG for the permission to publish the settlement data. Thanks are also extended to Dr. Giovanni Lombardi (Lombardi SA, Engineering Consultants) for his input and numerous discussions to clarify the scope of the work performed. Thanks are also extended to Dr. Nick Koutsabeloulis and the VIPS staff for their assistance with the VISAGE finite-element code.

References

[1] Zangerl C. Analysis of surface subsidence in crystalline rocks above the Gotthard highway tunnel, Switzerland. PhD thesis, ETH Zurich; 2003. 190p.

[2] Itasca. UDEC–universal distinct element code, version 3.1. Minneapolis: Itasca Consulting Group; 2000.

[3] Zangerl C, Eberhardt E, Loew S. Ground settlements above tunnels in fractured crystalline rock: numerical analysis of coupled hydromechanical mechanisms. Hydrogeol J 2003;11(1):162–73.

[4] Zangerl C, Loew S, Eberhardt E. Structure, geometry and formation of brittle discontinuities in anisotropic crystalline rocks of the Central Gotthard Massif, Switzerland. Eclogae Geol Helv 2006;99:271–90.

[5] Zangerl C, Evans KF, Eberhardt E, Loew S. Normal stiffness of fractures in granitic rock: a compilation of laboratory and in-situ experiments. Int J Rock Mech Min Sci 2008, in press, doi:10.1016/j.ijrmms.2008.02.001.

[6] Bandis SC, Lumsden AC, Barton NR. Fundamentals of rock joint deformation. Int J Rock Mech Min Sci 1983;20(6):249–68.

[7] Evans KF, Kohl T, Rybach L, Hopkirk RJ. The effects of fracture normal compliance on the long term circulation behaviour of a Hot Dry Rock reservoir: a parameter study using the new fully-coupled code FRACTure. Trans Geotherm Resources Council 1992;16: 449–56.

[8] Jung R. Hydraulic in situ investigations of an artificial fracture in the Falkenberg granite. Int J Rock Mech Min Sci 1989;26(3–4):301–8.

[9] Yoshinaka R, Yoshida J, Arai H, Arisaka S. Scale effects on shear strength and deformability of rock joints. In: Pinto da Cunha A, editor. Proceedings of the 1st international workshop on scale effects in rock masses, Lisbon. Rotterdam: Balkema; 1993. p. 143–9.

[10] Barton N. The shear strength of rock and rock joints. Int J Rock Mech Min Sci 1976;13(9):255–79.

[11] Byerlee JD. Friction of rocks. Pure Appl Geophys 1978;116(4–5): 615–26.

[12] Ehrbar H, Pfenniger I. Umsetzung der Geologie in technische Massnahmen im Tavetscher Zwischenmassiv Nord. In: Loew S, Wyss R, editors. Vorerkundung, und Prognose der Basistunnels am Gotthard und am Lötschberg, Zurich. Rotterdam: Balkema; 1999. p. 381–94.

[13] Luetzenkirchen VH. Structural geology and hydrogeology of brittle fault zones in the central and eastern Gotthard massif, Switzerland. PhD thesis, ETH Zurich; 2003. 264p.

[14] Kastrup U, Zoback ML, Deichmann N, Evans KF, Giardini D, Michael AJ. Stress field variations in the Swiss Alps and the northern Alpine foreland derived from inversion of fault plane solutions. J Geophys Res 2004;109(B01402).

[15] VIPS. VISAGE—vectorial implementation of structural analysis and geotechnical engineering, version 8.7. Bracknell, UK: Vector International Processing Systems Limited; 2003.

[16] Eberhardt E, Evans K, Zangerl C, Loew S. Consolidation settlements above deep tunnels in fractured crystalline rock: numerical analysis of coupled hydromechanical mechanisms. In: Stephansson O, et al., editors. Coupled thermo-hydro-mechanical-chemical processes in geo-system. Amsterdam: Elsevier; 2004. p. 759–64.

[17] Ebneter F. Geodätische Überwachung Sedrun-Faido. Geologie und Geotechnik der Basistunnels am Gotthard und am Lötschberg. In: Loew S, editor. Proceedings of the symposium geologie AlpTransit, Zürich. Zürich: vdf Hochschulverlag AG; 2006.

[18] Jones M, Mathiesen E. Pore pressure change and compaction in North Sea chalk hydrocarbon reservoirs. Int J Rock Mech Min Sci 1993;30(7):1205–8.

[19] Mossop A, Segall P. Subsidence at the Geysers geothermal field, N. California from comparison of GPS and levelling surveys. Geophys Res Lett 1997;24(14):1839–42.